Simultaneous Measurement of Surface Tension and Viscosity Using a Liquid Dynamics Sensor

*Naruhito Seimiya, Kuniharu Takei**

N. Seimiya, K. Takei
Graduate School of Information Science and Technology, Hokkaido University, Sapporo, Hokkaido 060-0814, Japan
takei@ist.hokudai.ac.jp

Keywords: liquid dynamics, surface tension, viscosity, reservoir computing, echo state network

The dynamics of liquids upon impact with an object exhibit distinctive behaviors influenced by physical parameters such as surface tension and viscosity, which can be determined by analyzing a liquid's dynamic response. However, measuring these parameters typically requires different tools, complicated setup, increased space, and higher costs. To streamline this process, we propose a liquid dynamic sensor capable of simultaneously extracting surface tension and viscosity via a single-step measurement. The proposed measurement method uses a superhydrophobic sensor comprising three electrode pairs, which were fabricated using laser-induced graphene on polydimethylsiloxane. The sensor monitors time-series resistance changes triggered by liquid impact dynamics. Our results showed that time-series liquid dynamics on the sensor surface vary with liquid's surface tension and viscosity, allowing for the differentiation of these properties. By implementing an echo state network algorithm, we successfully estimated surface tension and viscosity simultaneously. In addition, the system demonstrated reliable generalization capability, accurately estimating the properties of unknown liquids, which confirms the proposed sensor's robustness for simultaneous measurement of liquid physical parameters.

1. Introduction

The dynamics of a liquid impacting a surface are influenced by physical parameters such as viscosity, surface tension, and density. Monitoring the time-series dynamics of a liquid can facilitate the extraction of these physical parameters. However, distinguishing physical parameters solely by observing shape changes or droplet behaviors is challenging. Machine learning offers robust techniques for pattern recognition, classification, and prediction. Recently, researchers have employed reservoir computing (RC), a recurrent neural network architecture, to analyze time-series conductance and extract droplet volume and wind flow data by observing water droplet impacts on paired electrodes, effectively functioning as a weather sensor.[1] This finding highlights that liquid dynamics carry information that is influenced by environmental conditions. Because wind conditions alter water dynamics, properties such as viscosity and surface tension should also impact liquid dynamics during surface impact. To exploit these properties for parameter extraction through RC, sensor design is crucial for capturing time-series liquid dynamics because these parameters influence droplet spreading on solid surfaces.[2–7]

Viscosity measurements for small liquid volumes typically relies on detecting vibration amplitude differences under ultrasonic application, which is a commercially available method. This approach demonstrates that liquid dynamics is viscosity-dependent, suggesting that viscosity likely influences impact dynamics as well. Conversely, surface tension measurement requires a distinct method that often involves observation of a droplet's shape formed at a needle's tip. This indicates that liquid dynamics is surface tension-dependent, as observed in conventional shape-based measurements. Although surface tension and viscosity are essential properties for printing applications, they are traditionally measured by separate techniques, which are time-consuming, require additional measurement equipment, and increase costs. A single measurement unit capable of simultaneously capturing both parameters would provide substantial advantages over conventional approaches.

This study presents a method for simultaneously extracting surface tension and viscosity by measuring time-series conductivity changes using three superhydrophobic electrode pairs. These electrodes track dynamic changes in a liquid droplet upon impact on the electrode surfaces through conductivity variations, which are then analyzed using a developed RC algorithm to extract individual surface tension and viscosity values. To build training datasets for the echo state network (ESN), a type of RC platform, we measured different liquids, including water, isopropanol alcohol (IPA), ethanol, and glycerol, and their varying concentrations.[8–10] In addition, to investigate the effects of varying liquid properties, we captured time-series liquid behavior using a high-speed camera. The optimized ESN algorithm estimated both the viscosity and surface tension with high accuracy. The algorithm's generalization capability was evaluated by testing its accuracy on droplets of unknown liquids not included in the training data.

2. Results and discussion

2.1. Liquid droplet behaviors

Laser-induced graphene (LIG)[1, 12–16] was transferred from a polyimide (PI) film to polydimethylsiloxane (PDMS). Superhydrophobic surfaces on LIG electrodes and PDMS were created through laser texturing, resulting in rough surfaces that quickly repel liquids. The detailed procedures are described in the Methods section and Figure S1. Three pairs of electrodes, labeled as Ch1, Ch2, and Ch3 in increasing distance from the center, were fabricated based on the design in **Figure 1**a and 1b. Each electrode has a 0.5 mm gap and width. The concentric LIG/PDMS pattern without channel connections maintains circular symmetry, which prevents asymmetric liquid dynamics. Upon droplet impact, a closed electrical circuit forms as the droplet spreads, beginning at Ch1, and resistance changes at each channel are measured (Figure 1c). The measurement setups are described in the Methods section.

Depending on the liquid's physical properties on the sensor surfaces, time-series resistance changes reflect the liquid droplet's behavior upon contact with the electrodes (Figure 1c).

To confirm that dynamic changes depend on surface tension and viscosity, the liquid behavior upon impact with sensor surfaces was observed using a high-speed camera. Liquids with viscosities within 0.91–2.35 mPa·s and surface tensions within 31.1–71.4 $mN \cdot m^{-1}$ were measured using commercial tools (Table 1). Droplets of 15 μL were released from a 0.15-m height onto the sensor. The dynamic behaviors of different liquids are shown in **Figure 2**a and S2. First, water and 20 wt% IPA, which substantially differ in surface tension and viscosity, were compared (Figure 2a). Due to IPA's low surface tension, its droplet continued spreading immediately after impact without contracting, while the higher surface tension of water caused it to form smaller droplets that shrank and bounced on the sensor. These differences in wetting and liquid behavior suggests that time-series resistance changes would also vary, allowing for extraction of liquid parameters. Further systematic observations focused on the diameter change of liquid droplets after impact, using the normalized spreading diameter $\beta = D / D_0$ as a function of normalized time (τ), where D is the diameter at the measured time after impact, D_0 is the initial diameter at the moment of impact [6], and τ is calculated as follows:

$$\tau = v \times T/D_0, \qquad (1)$$

where v is the liquid's impact velocity and T denotes time. The droplet was assumed to be in free fall and calculated the velocity using a gravitational constant of 9.8. Neglecting the effects of air resistance and other factors, the velocity was calculated to be approximately 1.71 m s^{-1}. Figure 2b–d display results for varying water concentrations in IPA, ethanol, and glycerol, with water included in Figure 2d for comparison.

The droplet spreading process upon impact is divided into several phases: the kinematic phase ($\beta < 1$), spreading phase ($1 < \beta \leq \beta_{max}$), and relaxation equilibrium or degeneracy phase ($\beta_{max} < \beta$) [6,7]. The physical parameters and sensor surface roughness had a more pronounced

effect when $\beta > 1$[2–5]. Notably, for $\beta < 1$, the spreading rate (β) varied minimally across droplets; however, for $\beta > 1$, each droplet exhibited distinct spreading trends. In particular, for $\beta_{max} < \beta$, the degeneracy rate substantially varied with the surface tension, viscosity, and sensor surface wettability. Droplets with high surface tension exhibit greater degeneracy due to the liquid-repellent effect of surface roughness. In contrast, lower surface tension reduced the degeneracy rate, with β *value for 20 wt% IPA stabilizing at approximately* β_{max}. In general, β_{max} decreases as viscosity increases.[2–5] However, in this study, an opposite trend was observed for water and glycerol solutions at 5, 10, and 20 wt%, which had similar surface tensions but different viscosities. This discrepancy may result from the influence of sensor surface roughness and droplet surface tension, which outweighed the viscosity effects on spreading due to the low viscosity of these liquids.

2.2. Sensor response

Because liquids on the sensor surface exhibited different droplet diameter behaviors, Ch1–Ch3 channel resistance changes were measured for all liquids (**Figure 3**a–c). Fifty data points were collected per droplet, with resistance values ranging from 0 to 5 MΩ recorded over 15 ms. Figure 3a–c show the average time-series resistance changes for these 50 data points, including standard deviations. Upon droplet contact with an electrode pair, the sensor's resistance decreased rapidly, then increased at rates that varied according to the liquid parameters. By correlating sensor data with droplet impact behaviors captured via a high-speed camera, we observed that the rapid resistance increase was due to a reduction in the contact area between the electrode pairs and droplet as the droplet contracted (Figure 2a, S2, and 3a–3c).

To further elucidate the effect of penetration depth on the resistance changes in each flow channel, the relationship between the minimum resistance and the impact energy E_{impact} was investigated when droplets were dropped from different heights. The impact energy E_{impact} is expressed by the following equation:

$$E_{impact} = E_{kine} + E_{surf,} \quad (2)$$

where E_{kine} is the kinetic energy and E_{surf} is the surface energy of the droplet [11]. The terms on the right side are expressed as follows:

$$E_{kine} = \frac{1}{2}\rho_d V U^2 , \quad (3)$$

$$E_{surf} = \pi d_0^2 \sigma_{ig}, \quad (4)$$

where ρ_d, V, U, d_0, and σ_{ig} represent the droplet density (kg·m^{-3}), droplet volume (m^3), impact velocity to the sensor (m·s^{-1}), droplet diameter (m), and surface energy density of the liquid (J·m^{-2}), respectively.

The impact velocity was calculated by assuming free fall and using the gravitational acceleration of 9.8 m·s^{-2}. For each drop height, ten data were collected by dropping droplets with a glycerol concentration of 10 wt% (Figure S3a). The minimum resistance as a function of the impact energy in each channel is shown in Figures S3b-d.

In Ch1, although there was some variation due to slight deviations in the impact position, no clear trend was observed between the minimum resistance and the impact energy. On the other hand, in Ch2 and Ch3, the minimum resistance decreased as the impact energy increased (i.e., with higher drop heights). These results suggest that Ch1 is located at the impact center, where the droplet is already deeply embedded in the sensor at a drop height of 150 mm, making the influence of changes in impact energy relatively small. In contrast, Ch2 and Ch3 are positioned farther from the impact center, and as the impact energy increases, the droplet penetrates the sensor more deeply, resulting in a decrease in resistance. These findings indicate that as the distance from the impact point increases, the contact area between the droplet and the sensor has a significant influence on the resistance value.

When the droplet impacts the sensor, it spreads radially across the plane and exerts a vertical force, causing it to partially sink into the rough surface (Figure 3d). The droplet's surface tension and viscosity influence the sink depths, denoted as H_1 and H_2 (Figure 3d), and their

respective change ratios. As the droplet moves away from the impact point, the vertical force exerted on the sensor decreases, resulting in a shallower sink depth for droplets with higher surface tension (*i.e.,* $H_1 > H_2$) (Figure 3d).

Because the resistance changes as a fucntion of contact area between the electrodes and liquid, resistanace increased as the droplet moved away from the impact point and in cases with higher surface tension. The gradual resistance change likely corresponds to a reduction in droplet sinking depth, while sudden resistance changes are primarily attributed to a decrease in the horizontal contact area. These observations align well with the measured resistance data and high-speed camera images.

The 10 wt% ethanol solution, which had a higher viscosity and slightly lower surface tension compared to the 5 wt% IPA solution, exhibited a prolonged gradual resistance increase at Ch2 and Ch3. Similarly, in the case of water and glycerol solutions with 5, 10, and 20 wt% concentrations, the gradual resistance increase became more extended with higher viscosity. These observations indicate that viscosity reduces the droplet's receding speed. The resistance changes recorded across the three electrode pairs, based on surface tension and viscosity, demonstrate the sensor's ability to detect and differentiate these properties through time-series resistance changes droplet impact.

2.3. Surface tension and viscosity estimations

To estimate surface tension and viscosity simultaneously, two separate ESNs were developed using the same model structure but optimized with distinct hyperparameters and preprocessing techniques to address each property independently (**Figure 4**a). The target values for surface tension ($\hat{y}_{\mathrm{surf}}$) and viscosity ($\hat{y}_{\mathrm{vis}}$), along with the estimated ouputs for surface tension (y_{surf}), and viscosity ($\mathrm{y}_{\mathrm{vis}}$), were defined, and the ESN hyperparameters were optimized accordingly. A detailed description of the ESN model and analysis method is provided in the Methods section. Each liquid sample yielded 50 sensor data samples, which were divided into

30 training and 20 test data samples. To enhance generalization and prevent overfitting, Gaussian noise with a mean of 0 and a standard deviation of 0.02 was added to the training set, expanding it to 3,000 training data samples in total. In addition, to account for variations in droplet conductivity, a preprocessing step normalized both the training and test data using maximum ($R_{\max}$) and minimum (R_{mini}) resistance values. For data with slow resistance changes, the maximum resistance over time was set to $R_{\max}$, while for data with rapid resistance changes, $R_{\max}$ was set to

$$R_{\max} = R_{\mathrm{minimum}} + R_{\mathrm{x}}, \quad (5)$$

where the threshold resistance R_x is a hyperparameter related to the system performance. Resistance values exceeding $R_{\max}$ were set to $R_{\max}$. By adjusting R_x, the normalization process effectively highligted segments of the resistane pattern that were sensitive to surface tension or viscosity effects.

Additionally, the data segment lengths played a crucial role in optimizing the normalization process for accurate property estimation. Based on the grid search results, specific parameter values were selected for estimating surface tension and viscosity. For surface tension, normalized data with R_x = 2.2 MΩ and a data length of 11 ms was adopted (Figure S3a–c). For viscosity, normalized data with R_x = 0.9 MΩ and a data length of 13 ms was employed (Figure S3d–f). The surface tension estimation prioritized rapid resistance changes, while viscosity estimation emphasized gradual resistance changes.

To achieve optimal results, data normalization hyperparameters (threshold resistance R_x and data length L) and ESN hyperparameters (reservoir nodes N_x, learning time T, spectral radius SR, input magnitude IM, and leaky rate α) were optimized separately for surface tension and viscosity via grid search (Figure S4 and S5). Here, T refers to the collection time for reservoir nodes in spatial multiplexing (detailed in the Methods section). Parameters yielding the lowest normalized mean square error (NMSE) were selected as the optimal parameters. First,

the optimal R_x and L values were determined, and then the ESN hyperparameters were optimized through grid search using these values. The grid search revealed that the optimal hyperparameters for surface tension estimation were: R_x = 2.2 MΩ, L = 110 steps, N_x = 30, T = 27 steps, SR = 0.4, IM = 1.9, and α = 0.8. For viscosity estimation, the best parameters were R_x= 0.9 MΩ, L = 130 steps, N_x= 15, T = 32 steps, SR = 0.6, IM = 2.4, and α = 0.2. Figure 4b–c illustrates the results of surface tension and viscosity estimations with these optimized hyperparameters. The solid line indicates where the estimated values match the target values. Despite minor estimation errors, the accuracy for both sets of parameters is relatively high (Table1). Further quantitative evaluation will be discussed later. This slight variation in accuracy may be due to minor misalignments between the droplet and sensor positions during data collection. This issue could be mitigated by refining the measurement setup for better precision.

The generalization capability of the ESN algorithm to estimate parameters of unknown liquids—those not included in the training data—was evaluated. Optimized ESNs were trained using sensor data, excluding 5 wt% IPA, 5 wt% glycerol, and 10 wt% ethanol, and then applied to estimate these unknown liquid's surface tension and viscosity (Figure 4d and 4e). The solid lines in Figure 4d-e represent the diagonal, indicating where the estimated values are equal to the target values.The estimated values for 5 wt% IPA were surface tension 50.4±3.24 $mN{\cdot}m^{-1}$ and viscosity 1.39±0.138 mPa·s; for 5 wt% glycerol, surface tension 70.5±2.96 $mN{\cdot}m^{-1}$ and viscosity 1.03±0.131 mPa·s; and for 10 wt% ethanol, surface tension 51.3±4.04 $mN{\cdot}m^{-1}$ and viscosity 1.41±0.145 mPa·s. The results showed that the sensor system could estimate surface tension and viscosity for unknown liquids with values close to the measured ones, achieving reasonable accuracy, although there was a slight increase in variablity compared to the trained samples. This variability could be reduced by expanding the dataset in future studies.

Nevertheless, it is practically challenging to cover all possible droplet types. These findings demonstrate that the sensor system can generalize to estimate unknown data within a surface

tension range of 31.1–71.4 mN·m^{-1} and a viscosity range of 0.91–2.35 mPa·s, as long as the properties of the unknown liquids fall within these bounds. Additional measurements and training would be necessary to extend the system's estimation capabilities to liquids with lower surface tension or higher viscosity. This study confirms that the sensor system exhibits high generalization capability even with a limited amount of training data, indicating that training on all possible droplet types under specific conditions is not necessary. However, if the properties of a new liquid differ significantly from the existing dataset, additional training may be required.

To quantitatively assess the effectiveness of the ESN algorithm, NMSE was used to evaluate system performance as follows:

$$\mathrm{NMSE} = \frac{\sum_{i=1}^{M}(y_i - \hat{y}_i)^2}{\sum_{i=1}^{M}(\hat{y}_i - \bar{y}_i)^2}\ , \qquad (6)$$

where y_i, $\hat{y}_i$, and $\bar{y}_i$ denote the estimated, target, and average target values, respectively. The NMSEs were calculated for surface tension and viscosity estimations both with and without ESN. Detailed analysis of the results obtained without ESN is provided in the Supporting Information. The NMSE for surface tension estimation using the ESN was over 1.8 times lower, and for viscosity estimation, it was 1.7 times lower than the results without the ESN (Table 2 and Figure S6). For example, the estimated values for 5 wt% IPA were surface tension 49.5±3.83 mN·m^{-1} and viscosity 1.34±0.113 mPa·s; for 5 wt% glycerol, surface tension 70.2±4.38 mN·m^{-1} and viscosity 1.04±0.106 mPa·s; and for 10 wt% ethanol, surface tension 49.1±3.83 mN·m^{-1} and viscosity 1.38±0.125 mPa·s. This reduction in error highlights the effectiveness of the ESN's nonlinearity and high dimensionality in enabling the effective linear separation of sensor data for both surface tension and viscosity estimations. Notably, the estimations without the ESN still showed reasonable accuracy, with values close to the actual measurements, indicating that the sensor data inherently carry valuable information. To further explore the influence of the ESN on estimation accuracy, we compared the NMSE of the ESN

using only data from the collision center channel (Ch1) with that obtained from others (Figure S7). The ESN with only Ch1 input data showed lower accuracy compared to the three-channel configuration without the ESN (Table 2, Figure S6 and S7). This result suggests that tracking the temporal spread across multiple channels on the sensor surface is essential for accurately extracting both surface tension and viscosity information simultaneously.

The stability of this sensor is crucial for practical applications. First, the stability of the sensor was evaluated by examining changes in its performance over time after fabrication. Figure S9a shows the time-series resistance changes of 10 wt% glycerol using sensors on day 1, day 10, after 2 weeks, and after 4 months. Here, data were measured 10 times each. Figures S9b-c present the estimated surface tension and viscosity results. On day 1, the estimated surface tension was 68.2±2.09 $mN \cdot m^{-1}$ (NMSE = 0.0009354), and the viscosity was 1.27±0.0652 mPa·s (NMSE = 0.002889). On day 10, the estimated surface tension was 67.4±1.34 $mN \cdot m^{-1}$ (NMSE = 0.0005423), and the viscosity was 1.27±0.0649 mPa·s (NMSE = 0.003041). After 2 weeks, the surface tension was 66.0±2.62 $mN \cdot m^{-1}$ (NMSE =0.002596), and the viscosity was 1.24±0.0646 mPa·s (NMSE = 0.004933), while after 4 months, the values were 65.3±2.23 $mN \cdot m^{-1}$(NMSE = 0.002934) and 1.35±0.0842 mPa·s (NMSE = 0.005882), respectively. The results of the NMSE analysis showed that the error increased after 2 weeks; however, it did not significantly increase beyond 4 months (Figure S9d). Furthermore, the NMSE of the estimated values on day 10 was smaller than that on day 1, which is considered to be due to variations in the droplet impact position. Although the NMSE increased over time, the sensor was still able to provide relatively accurate estimates even after 4 months. However, to maintain high accuracy, it is recommended to replace the sensor every 2 weeks.

Next, the durability of the sensor under repeated droplet impacts was evaluated (Figure S10a). Here, data were measured 10 times in each cycle. Regarding sensor cleaning, residual liquid on the sensor surface was removed by blowing air. The measurements were conducted up to 200 cycles, and it was observed that the estimation error increased as the number of droplet

impacts increased (Figures S10b–c). Specifically, after 10 cycles, the estimated surface tension was 68.2±2.09 mN·m^{-1}(NMSE = 0.0009354) and the viscosity was 1.27±0.0652 mPa·s (NMSE = 0.002889); after 100 cycles, the surface tension was 66.9±2.13 mN·m^{-1} (NMSE = 0.001416) and the viscosity was 1.26±0.105 mPa·s (NMSE = 0.007685); and after 200 cycles, the surface tension was 67.8±2.95 mN·m^{-1} (NMSE = 0.001919) and the viscosity was 1.33±0.124 mPa·s(NMSE = 0.009411) (Figures S10d). These results suggest that the sensor's continuous measurement capability is limited to approximately 100 cycles. To ensure reliable performance, replacement is recommended after reaching this limit.

For further validation, the feasibility of estimating the surface tension and viscosity of a solution under different temperature conditions was investigated. In this study, the measurement results of water droplets at 18°C were examined. The measured values of surface tension and viscosity for 18°C water droplets were 72.2 mN·m^{-1} and 1.09 mPa·s, respectively. Using 10 data points, the estimated values and NMSE were determined as 71.5 ± 3.50 mN·m^{-1} (NMSE = 0.002444) for surface tension and 1.10 ± 0.103 mPa·s (NMSE = 0.009006) for viscosity (Figure S11). In contrast, for water droplets at the training data temperature at 25°C, the estimated surface tension was 70.7 ± 1.51 mN·m^{-1} (NMSE = 0.0005470), and the estimated viscosity was 0.96 ± 0.0595 mPa·s (NMSE = 0.007639). In all temperature conditions, the NMSE for viscosity exhibited greater variability compared to surface tension. However, although the estimation accuracy slightly decreased under conditions different from the training data temperature, it was confirmed that surface tension and viscosity could still be estimated with sufficient accuracy.

3. Conclusions

This study successfully demonstrated a novel approach for simultaneously measuring liquid surface tension and viscosity by monitoring resistance changes resulting from liquid dynamics on a sensor equipped with three pairs of superhydrophobic electrodes. The use of a high-speed

camera allowed for a detailed examination of how liquid dynamics vary with surface tension and viscosity, leading to different time-series resistance trends across the sensor channels. To estimate these parameters from the time-series resistance changes, two ESN algorithms were utilized, yielding highly accurate estimations after careful optimization of data preprocessing, hyperparameters, and algorithmic configurations. Importantly, the sensor system was able to accurately estimate surface tension and viscosity for unknown droplets, demonstrating its robustness and strong generalization capability even without prior training on specific data. While further investigations, including studies on temperature dependence, are warranted to enhance the system's applicability, this method represents a notable advancement in simultaneous surface tension and viscosity measurements compared to conventional methods. The findings highlight the potential for this sensor system to provide valuable insights in various scientific and industrial applications where liquid properties are critical.

4. Experimental Section/Methods

4.1. Sensor fabrication

The sensor was fabricated using a programmable CO_2 laser cutter (VLS 2.30, Universal Laser System) to process a PI film(model number 3-1966-05 manufactured by AS ONE Corporation). The photothermal effect of the laser on the PI film resulted in the formation of LIG (Figure S1 (1)).[1, 12–16] The laser power was 10 W, with a speed of 254 mm/s at 500 pulses per inch (PPI). The wavelength of the laser is 10.6 μm and the beam size is about 76 μm. The distance between the sample and the laser was fixed at 2.3 mm. Following the LIG formation, a PDMS precursor liquid (Sylgard 184, Dow) was poured over the LIG/PI film and cured at 90°C for 90 min (Figure S1 (2)). After curing, the PDMS was carefully peeled off, transferring the LIG onto the PDMS substrate (Figure S1 (3)). To achieve a superhydrophobic surface, both the LIG/PDMS and PDMS surfaces were texturized via CO_2 laser by scanning, creating a random roughness resembling the Lotus effect as described by the Cassie–Baxter model (Figure

S1(4)).[1,16–17] For the texturization process, the laser power was set to 3.75 W at a laser scanning speed of 508 mm s^{-1} at 500 PPI.

4.2. Data measurements

A micropipette dispensed different liquids, with each droplet having a volume of 15 μL. The conductivity change in the channel was measured using a memory HiCoder (MR6000, HIOKI) at a sampling rate of 10 kHz.

4.3. Reference values of surface tension and viscosity

Surface tension and viscosity were measured 10 times at room temperature (~25℃) using commercial tools, and the average values were used as references for ESN estimations. Surface tension was measured using a commercial droplet measurement tool (SmartDrop Plus, Femtobiomed), whereas viscosity was measured using an ultrasonic-based viscosity (SV-10 Viscometer, AND).

4.4. Modeling and analysis of ESNs

The ESN is defined as $x(\mathrm{t}) \in \mathbb{R}^{N_x}$ with an initial state $x(0) = 0$ and is updated according to the following equation:

$$x(t) = (1-\alpha)\cdot x(t-1) + \alpha \cdot \tanh(Wx(t-1) + W_{in}[1; u(t)]), \quad (4)$$

where the leaky rate $\alpha \in (0,1]$ is a hyperparameter that determines the degree of change from the previous ESN state, and $u(\mathrm{t}) \in \mathbb{R}^{N_u}(N_u = 3)$ is the external input. A bias term is added to the input $u(\mathrm{t})$, which is preprocessed by normalization. The matrices $W_{in} \in \mathbb{R}^{N_x \times (1+N_u)}$ and $W \in \mathbb{R}^{N_x \times N_x}$ represent the input and internal weight matrices, respectively. Here, W_{in} is uniformly distributed over the range $[-\sigma, \sigma]$, where σ is the input magnitude, a hyperparameter. The spectral radius of W is also a hyperparameter that influences the dynamics

of the ESN. Next, the x(t) values over T learning time steps, collected at equal intervals from the input data length L, were reconstructed along the spatial direction as a node $s \in \mathbb{R}^{N_s}$ (where $N_s = N_x \cdot T$):

$$s = [x(1); x(2); \cdots; x(T)]. \quad (5)$$

Here, the collected $x(t)$ values were augmented with observational noise following a normal distribution with a standard deviation of 0.005 after updating to prevent multicollinearity in the learning of readout weights, which will be discussed later. The nodes s were then concatenated with a bias term for output and connected to the output layer:

$$S = [1; s] \in \mathbb{R}^{(N_s+1)}, \quad (6)$$

$$y = W_{out}S, \quad (7)$$

where $y \in \mathbb{R}^{N_y}(N_y = 1)$ and $W_{out} \in \mathbb{R}^{N_y \times (N_s+1)}$ represent the output and readout weight, respectively. Ridge regression was applied to learn the readout weights and prevent overfitting as follows:

$$W_{out} = (S^T S + \beta I)^{-1} S^T y\ , \quad (8)$$

where β denotes the ridge term that prevents overfitting and hyperparameter. When $\beta = 0$, the optimal W_{out} is $W_{out} = (S^T S)^{-1} S^T y$, obtained by least squares. As β approaches infinity, the optimal W_{out} approaches zero. In this study, the optimal β was determined by solving for the degrees of freedom (df) as follows[18]:

$$df = \sum_{i=1}^{N_s+1} \frac{\lambda_i}{\lambda_i + \beta}\ , \quad (9)$$

where $\{\lambda_i\}$ represents the eigenvalues of $S^T S$. The df varies from 1 to $N_s + 1$, and there is a corresponding β for each df. Both β and W_{out} were calculated for each df based on Equation (8) and (9). The residual sum of squares, given by RSS $= \sum_{k=0}^{M-1} (\hat{y} - y)^2$, was then calculated to determine Akaike's information criterion (AIC):

$$AIC = M \log(RSS) + 2\, df, \quad (10)$$

where M represents the training data size. $M = 3000$ and $M = 2100$ were used for learning across all droplet conditions and investigating generalization capability, respectively. Finally, the optimal β and W_{out} values were determined by minimizing AIC calculated for each df.

Supporting Information

Supporting Information is available from the Wiley Online Library or from the author.

Acknowledgements

This work was partially supported by JSPS KAKENHI (Grant No. JP22H00594, JP24H00887), JST ALCA-Next (Grant No. JPMJAN23F1), and the Murata Science Foundation.

Received: ((will be filled in by the editorial staff))
Revised: ((will be filled in by the editorial staff))
Published online: ((will be filled in by the editorial staff))

Conflict of Interest

The authors declare no competing interest.

Data Availability Statement

Data that support the findings of this study are available from the corresponding author on reasonable request.

References

[1] S. Wakabayashi, T. Arie, S. Akita, K. Nakajima, K. Takei, *Adv. Mater.* **2022**, 34, 2201663.

[2] S. Lin, B. Zhao, S. Zou, J. Guo, Z. Wei, L. Chen, *J. Colloid Interface Sci.* **2018**, 516, 86–97.

[3] C. Tang, M. Qin, X. Weng, X. Zhang, P. Zhang, J. Li, Z. Huang, *Int. J. Multiphase Flow* **2017**, 96, 56–69.

[4] J. B. Lee, N. Laan, K. G. de Bruin, G. Skantzaris, N. Shahidzadeh, D. Derome, J.

Carmeliet, D. Bonn, *J. Fluid Mech.* **2016**, 786, R4.

[5] J. Seo, J. S. Lee, H. Y. Kim, S. S. Yoon, *Exp. Therm. Fluid. Sci*. **2015**, 61, 121–129.

[6] M. Qin, C. Tang, S. Tong, P. Zhang, Z. Huang, *Int. J. Multiphase. Flow.* **2019**, 117, 53–63.

[7] R. Rioboo, M. Marengo, C. Tropea, *Exp. Fluids.* **2002**, 33, 112–124.

[8] M. Lukoševičius, "A Practical Guide to Applying Echo State Networks," in *Neural Networks: Tricks of the Trade*, 2nd ed., G. Montavon, G. B. Orr, K.-R. Müller, Eds., Springer, Berlin, Heidelberg, 2012, pp. 659–686.

[9] M. Lukoševičius, H. Jaeger, *Comput. Sci. Rev.* **2009**, 3, 127–149.

[10] K. Nakajima, I. Fischer, *Reservoir Computing*, Springer, Singapore, 2021.

[11] Y. Yonemoto, T. Kunugi, *Sci. Rep.* **2017**, 7, 2362.

[12] R. Ye, D. K. James, J. M. Tour, *Acc. Chem. Res.* **2018**, 51, 1609–1620.

[13] K. Xu, Z. Cai, H. Luo, Y. Lu, C. Ding, G. Yang, L. Wang, C. Kuang, J. Liu, H. Yang, *ACS Nano* **2024**, 18, 26435–26476.

[14] J. Lin, Z. Peng, Y. Liu, F. Ruiz-Zepeda, R. Ye, E. L. G. Samuel, M. J. Tacaman, B. I. Yacobson, J. M. Tour, *Nat. Commun*. **2014**, 5, 5714.

[15] K. Xu, Y. Fujita, Y. Lu, S. Honda, M. Shiomi, T. Arie, S. Akita, K. Takei, *Adv. Mater.* **2021**, 33, 2008701.

[16] K. Y. Law, *Acc. Mater. Res.* **2021**, 3, 1–7.

[17] X. He, K. Zhang, X. Xiong, Y. Li, X. Wan, Z. Chen, Y. Wang, X. Xu, M. Liu, Y. Jiang, S. Wang, *Small* **2022**, 18, 2203264.

[18] K. Nakajima, H. Hauser, T. Li, *Soft. Rob.* **2018**, 5, 339-347.

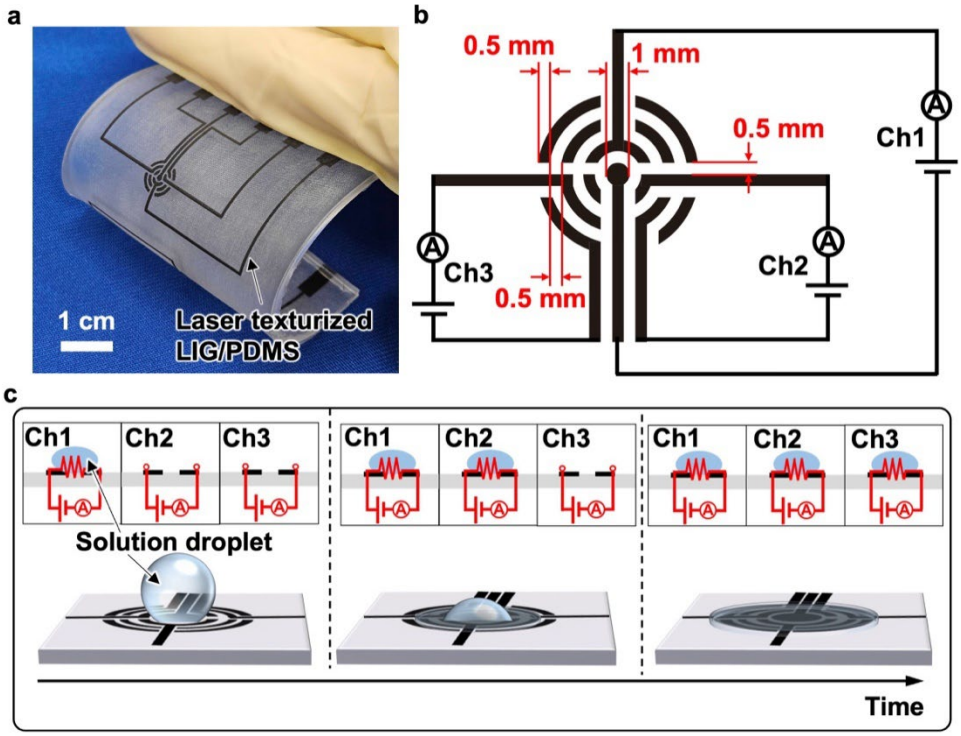

Figure 1. Sensor schematic and concept. (a) Photograph of liquid dynamics sensor designed for simultaneous surface tension and viscosity estimation. (b) Overview of the sensor design and channel assignments from Channel 1 (Ch1) to Channel 3 (Ch3). (c) Illustration of the sensing concept, depicting closed and opened circuits with and without liquid using three pairs of electrodes.

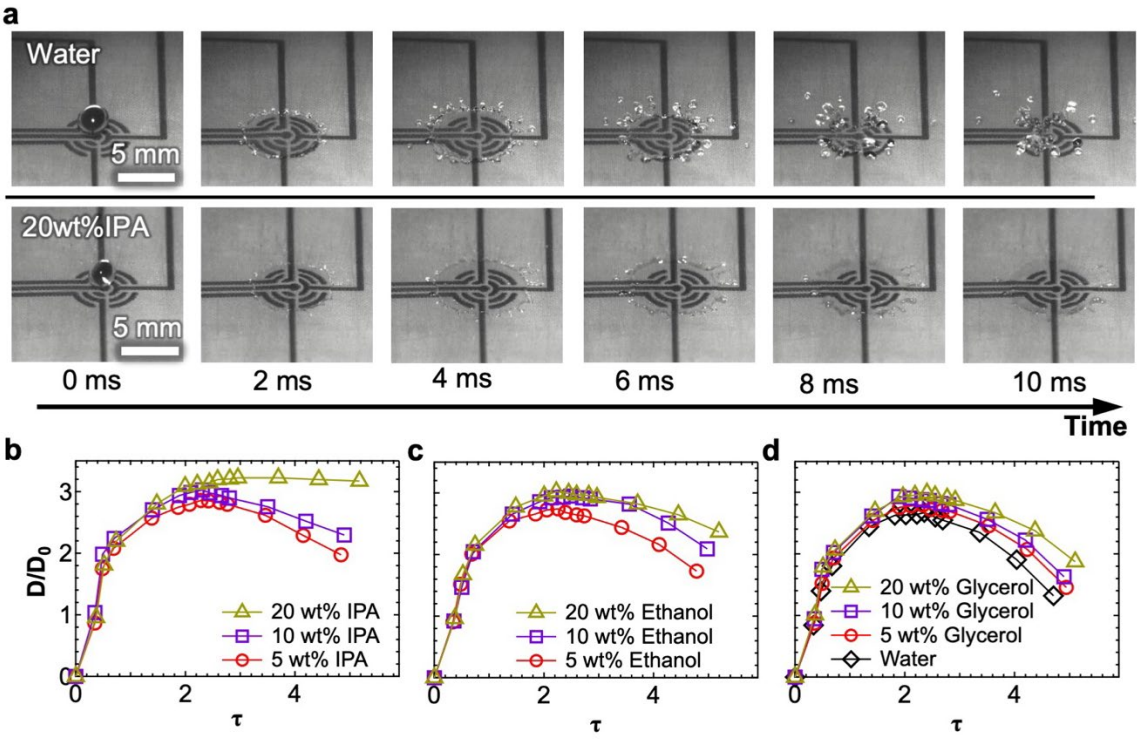

Figure 2. Liquid dynamics. (a) High-speed camera images capturing time-series liquid behaviors on LIG/PDMS for water and 20 wt% isopropyl alcohol (IPA). (b) Normalized droplet spreading diameter (D/D_0) plotted against normalized time (τ) for different IPA concentrations. (c) Normalized droplet spreading diameter (D/D_0) as a function of normalized time (τ) for different ethanol concentrations. (d) Normalized droplet spreading diameter (D/D_0) for water with varying glycerol concentrations.

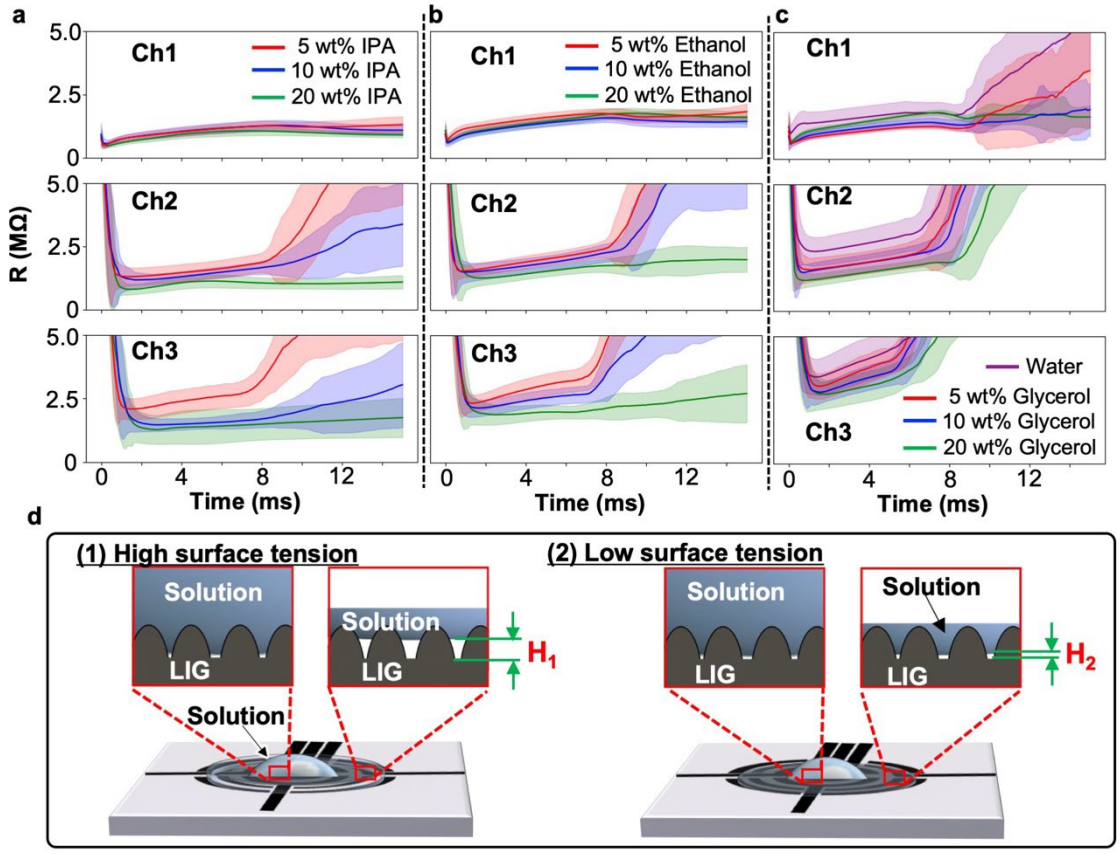

Figure 3. Sensor responses and sensing mechanism. (a)Time-series resistance changes with standard deviation for each channel (Ch1, Ch2, and Ch3) for different IPA concentrations. (b) Time-series resistance changes for different ethanol concentrations. (c) Time-series resistance changes for water with varying glycerol concentrations. (d) Illustration of the sensing mechanism showing dynamic resistance changes based on variations in surface tension and viscosity.

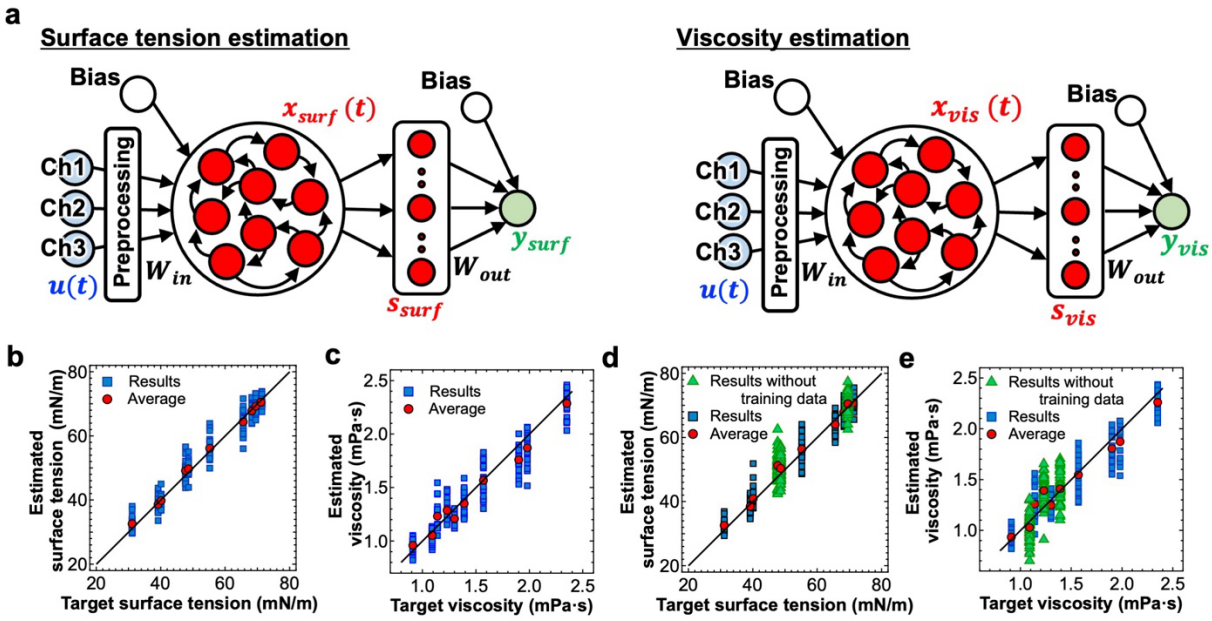

Figure 4. Simultaneous surface tension and viscosity estimations. (a) Schematics outlining the data processing using echo state network (ESN), including various preprocessing steps and hyperparameters for surface tension and viscosity estimations. (b) Comparison of estimated surface tension values with target values using ESN. (c) Comparison of estimated viscosity values with target values using ESN. (d) Estimated surface tension values for unknown liquids without prior training. (b)-(e) Solid lines indicate where the estimated values match the target values.

Table 1. Surface tension and viscosity values measured using commercial instruments and estimated by RC.

	Water	5wt% glycerol	10wt% glycerol	20wt% glycerol	5wt% ethanol	10wt% ethanol	20wt% ethanol	5wt% IPA	10wt% IPA	20wt% IPA
Measured Surface tension [mN/m]	71.4	69.5	68.3	65.6	55.2	48.6	39.2	47.7	40.1	31.1
Estimated Surface tension [mN/m]	70.6±1.7	69.3±2.0	67.8±2.4	64.4±3.8	56.2±3.5	49.8±2.3	38.7±2.4	49.2±3.0	39.8±2.0	32.6±2.2
Measured Viscosity [mPa·s]	0.91	1.09	1.30	1.90	1.14	1.39	1.98	1.23	1.57	2.35
Estimated Viscosity [mPa·s]	0.96±0.06	1.05±0.06	1.21±0.06	1.76±0.11	1.23±0.13	1.35±0.11	1.87±0.15	1.29±0.10	1.57±0.15	2.29±0.12

Table 2. Normalized mean squared error (NMSE) results for surface tension and viscosity estimations across different conditions.

	Surface tension			Viscosity		
	With ESN (3ch)	Without ESN (3ch)	With ESN (1ch)	With ESN (3ch)	Without ESN (3ch)	With ESN (1ch)
All data	0.002552	0.004638	0.01166	0.007575	0.01338	0.03066
Generalization performance	0.004136	-	-	0.01248	-	-

This study demonstrates simultaneous measurements of surface tension and viscosity of liquid by monitoring the time-series impact dynamics of a liquid using a superhydrophobic sensor consisting of three electrode pairs and an echo state network algorithm.

Naruhito Seimiya, Kuniharu Takei*

Simultaneous measurement of surface tension and viscosity using a liquid dynamics sensor

ToC figure ((Please choose one size: 55 mm broad × 50 mm high **or** 110 mm broad × 20 mm high. Please do not use any other dimensions))

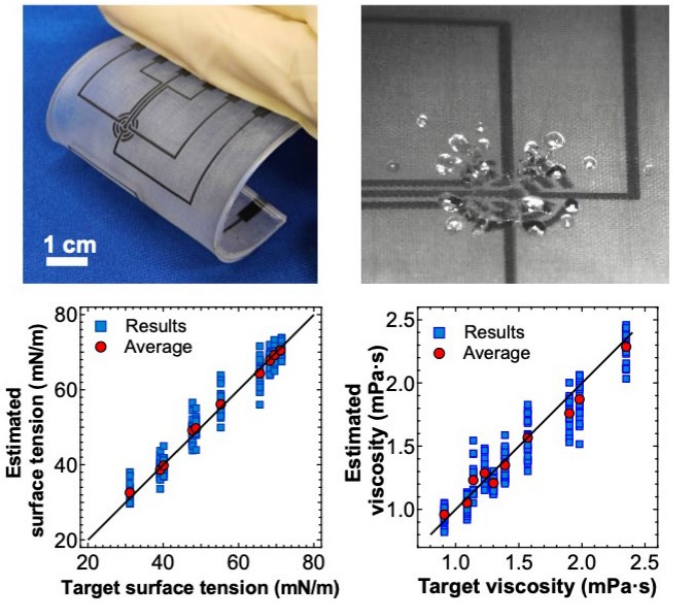

Supporting Information

Simultaneous measurement of surface tension and viscosity using a liquid dynamics sensor

*Naruhito Seimiya, Kuniharu Takei**

Data analyses without ESN

To test the effectiveness of echo state network (ESN), the estimated results obtained with ESN were compared with those obtained using ridge regression without ESN. In the ridge regression model without ESN, used to estimate the surface tension or viscosity of a droplet, the time-multiplexed node $U \in \mathbb{R}^{N_u \cdot T}$ is employed as follows:

$$U = [u(1); u(2); \cdots; u(T)]. \quad (1)$$

The input data u(t) for T learning time steps were collected at equal intervals from the input data length L and concatenated in the time direction. The output is then given by:

$$y = W_{out}[1; \mathrm{U}], \quad (2)$$

where the bias is connected to node U. Figure S6 shows the estimated surface tension and viscosity without using ESN.

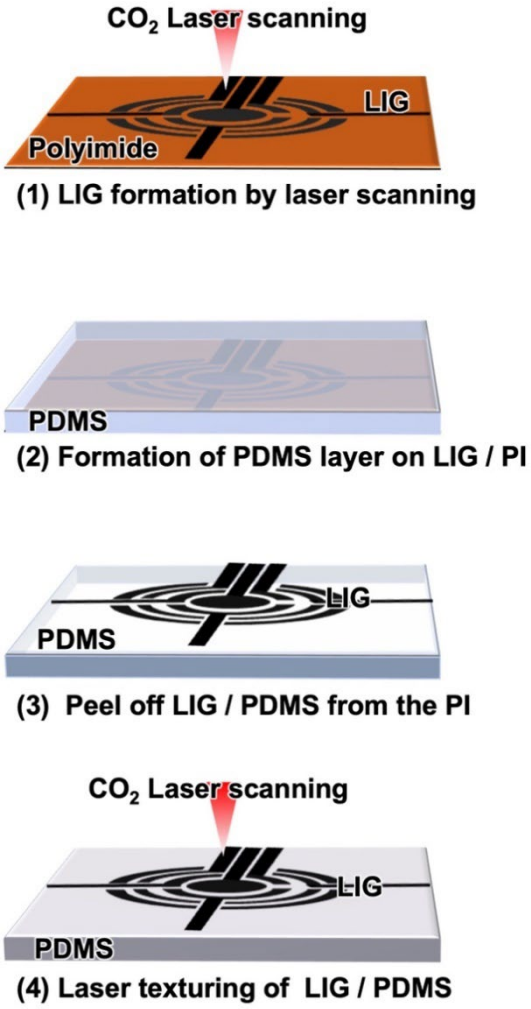

Figure S1. Sensor fabrication process.

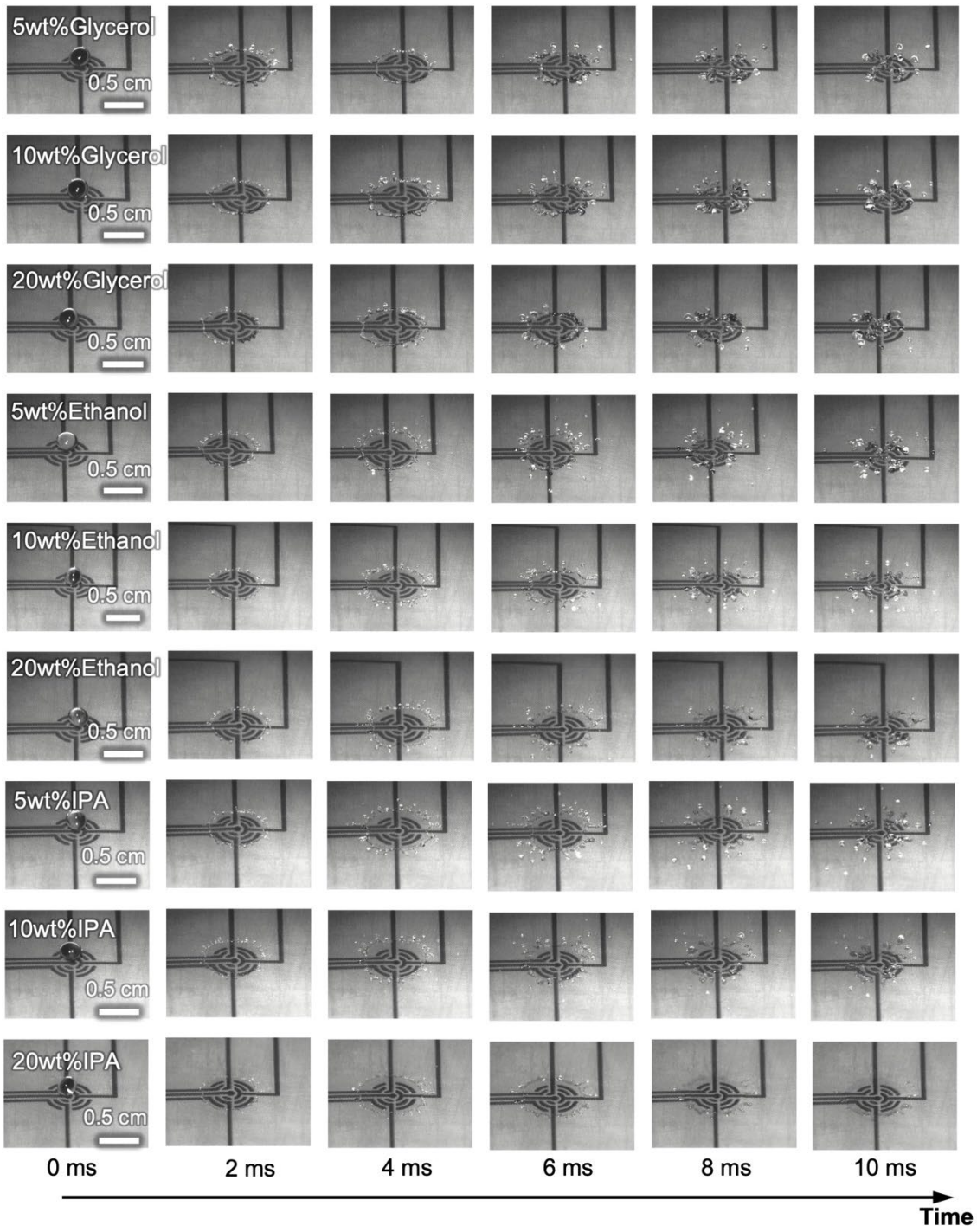

Figure S2. High-speed camera images of time-series liquid behaviors on LIG/PDMS.

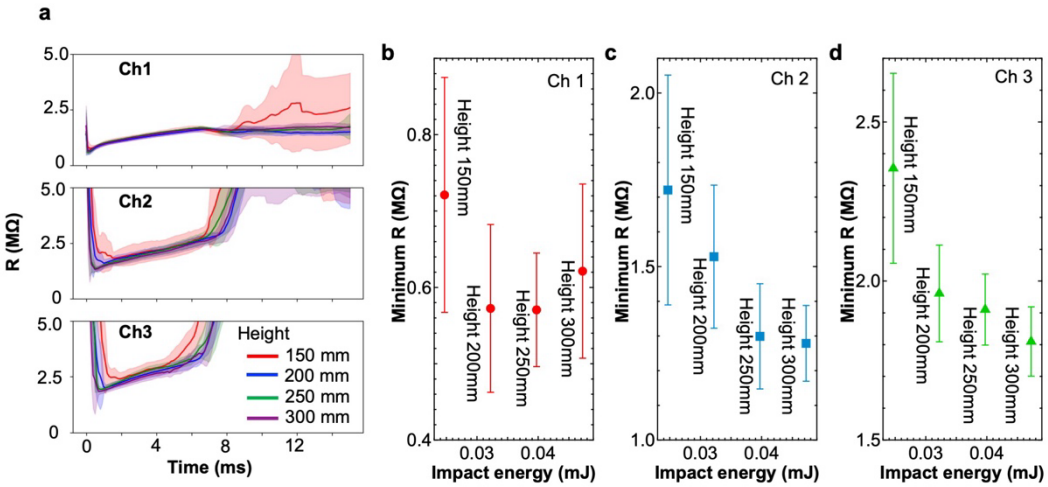

Figure S3. Resistance at Ch1, Ch2, and Ch3 at different height. (a) Time-series resistance changes with standard deviation for each channel (Ch1, Ch2, and Ch3) at different drop height for 10 wt% glycerol. The minimum resistance in (b) Ch1, (c) Ch2, and (d) Ch3 at different impact energy corresponding to different height.

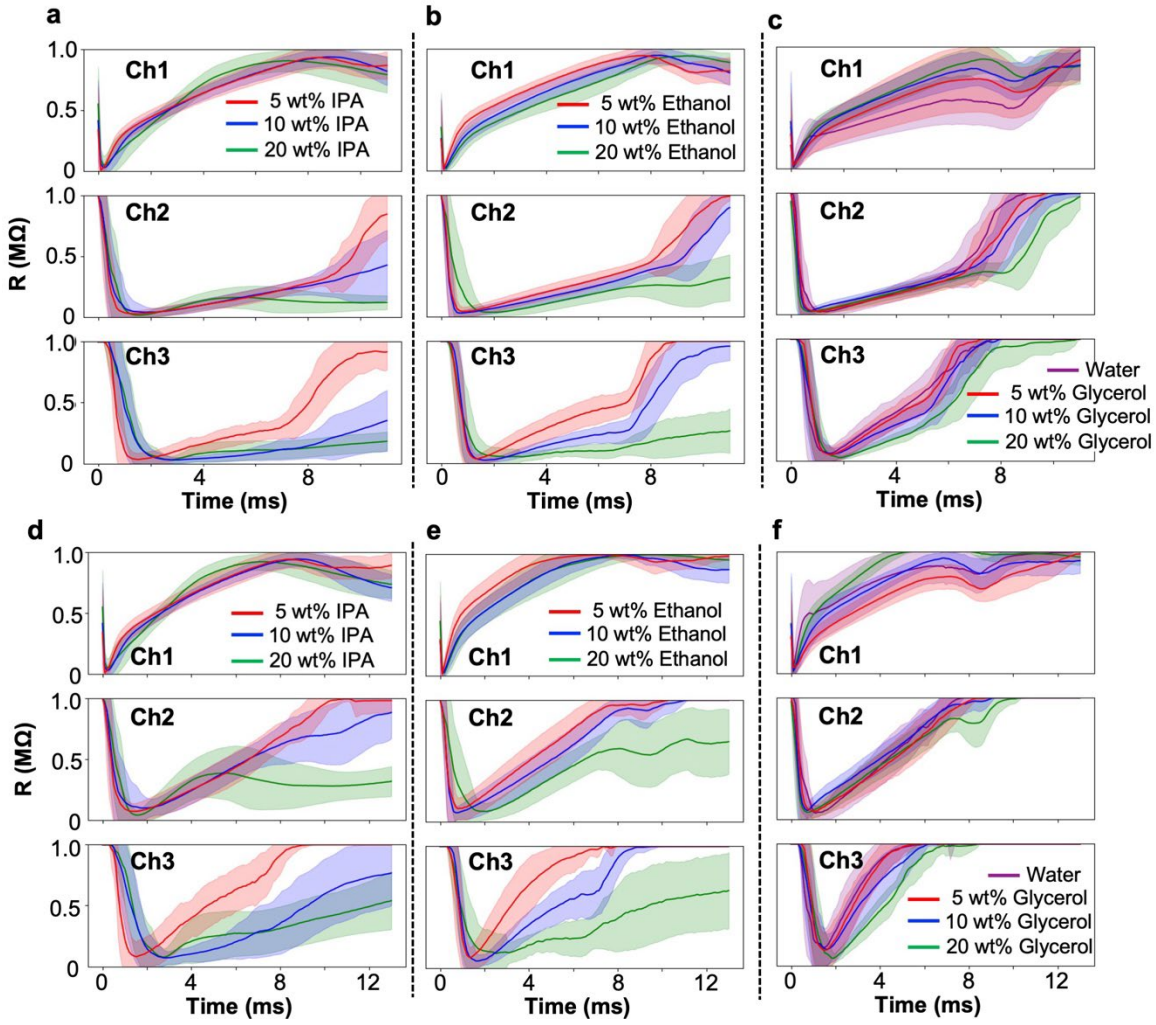

Figure S4. Sensor data after normalization and data augmentation. Normalized and augmented datasets for surface tension estimation: (a) IPA, (b) ethanol, and (c) water and glycerol. Normalized and augmented datasets for viscosity estimation: (d) IPA, (e) ethanol, and (f) water and glycerol.

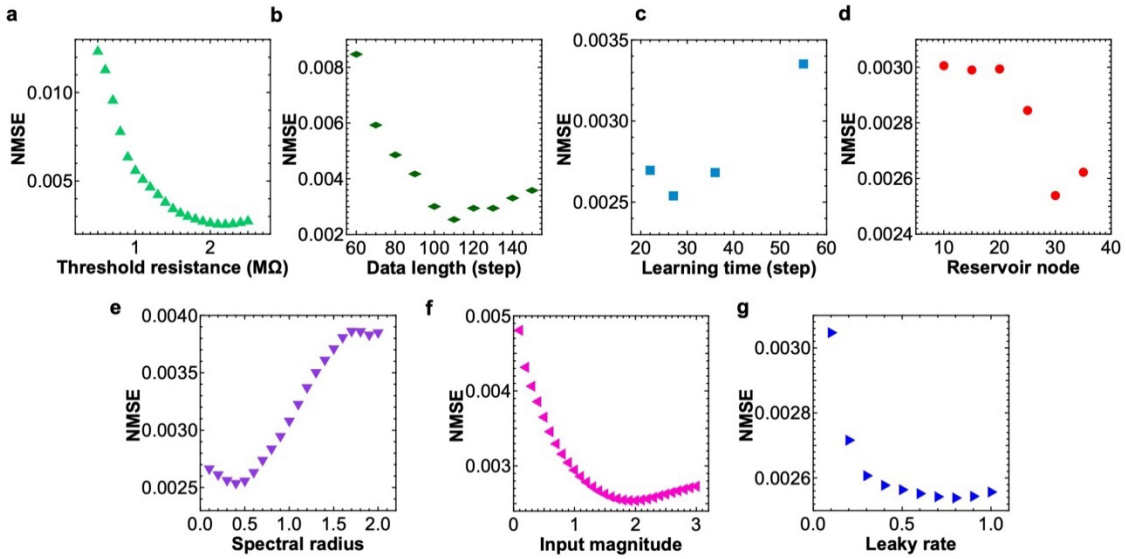

Figure S5. Optimization of hyperparameters for surface tension. Grid search results for surface tension estimation of (a) threshold resistance, (b) data length, (c) learning time, (d) reservoir node, (e) spectral radius, (d) input magnitude, and (e) leaky rate.

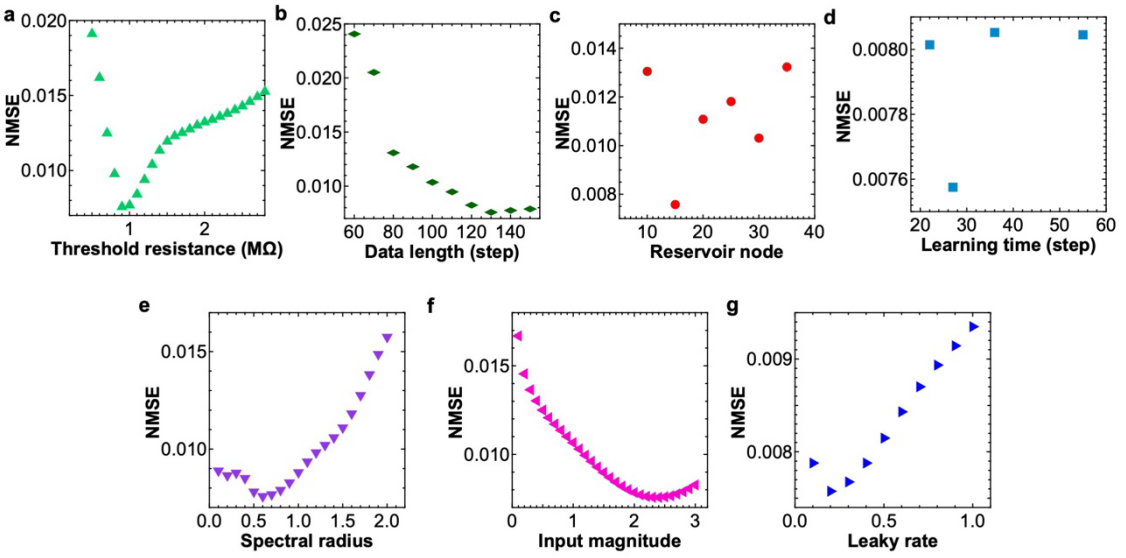

Figure S6. Optimization of hyperparameters for viscosity. Grid search results for viscosity estimation of (a) threshold resistance, (b) data length, (c) learning time, (d) reservoir nodes, (e) spectral radius, (d) input magnitude, and (e) leaky rate.

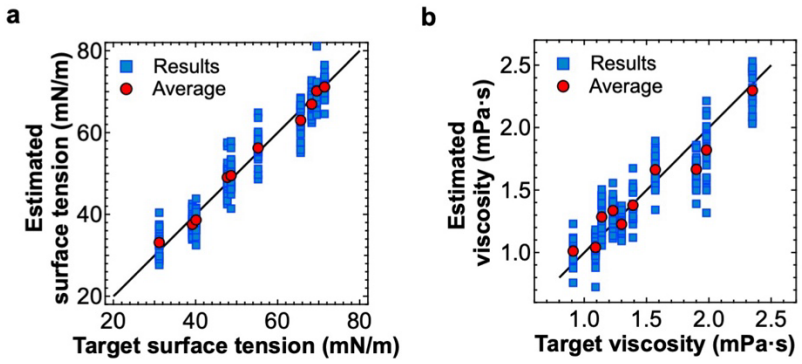

Figure S7. Estimation results without using ESN. (a) Surface tension and (b) viscosity estimated by ridge regression without using ESN.

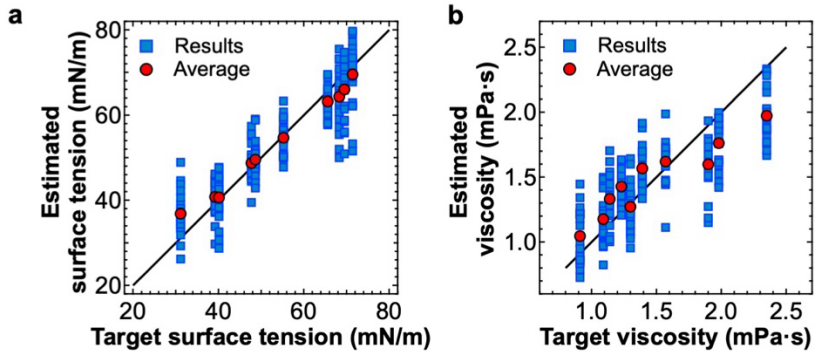

Figure S8. Estimation results using only one channel (Ch1). (a) Surface tension and (b) viscosity estimated using ESN from only Ch1 data.

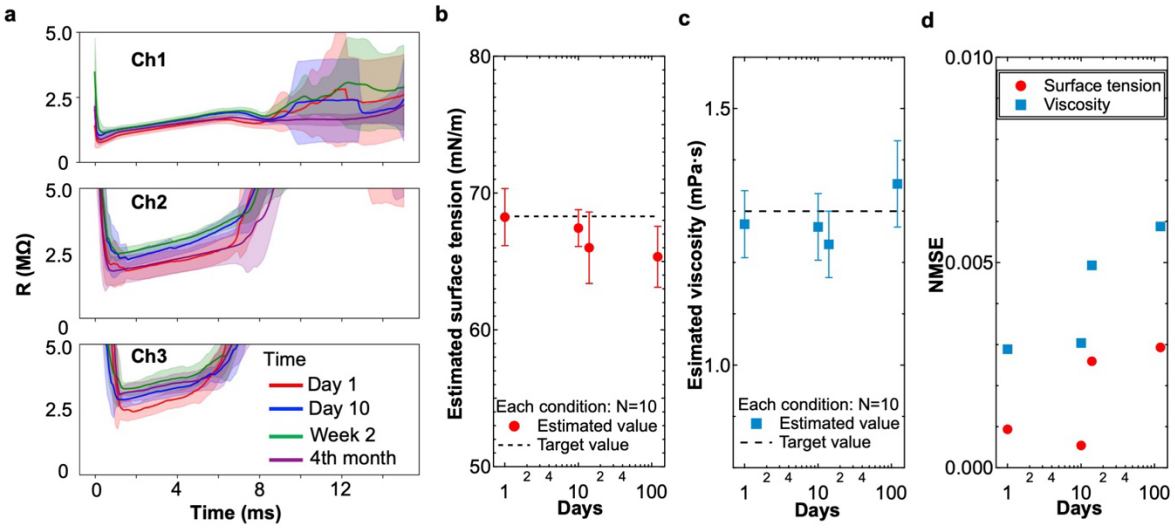

Figure S9. Sensor stability over time. (a) Time-series resistance changes with standard deviation for each channel (Ch1, Ch2, and Ch3) over time elapsed since sensor fabrication for 10 wt% glycerol. Comparisons of (b) estimated surface tension values and (c) estimated viscosity values over time elapsed since sensor fabrication for 10 wt% glycerol. (d) Changes in NMSE of surface tension and viscosity over time elapsed since sensor fabrication for 10 wt% glycerol.

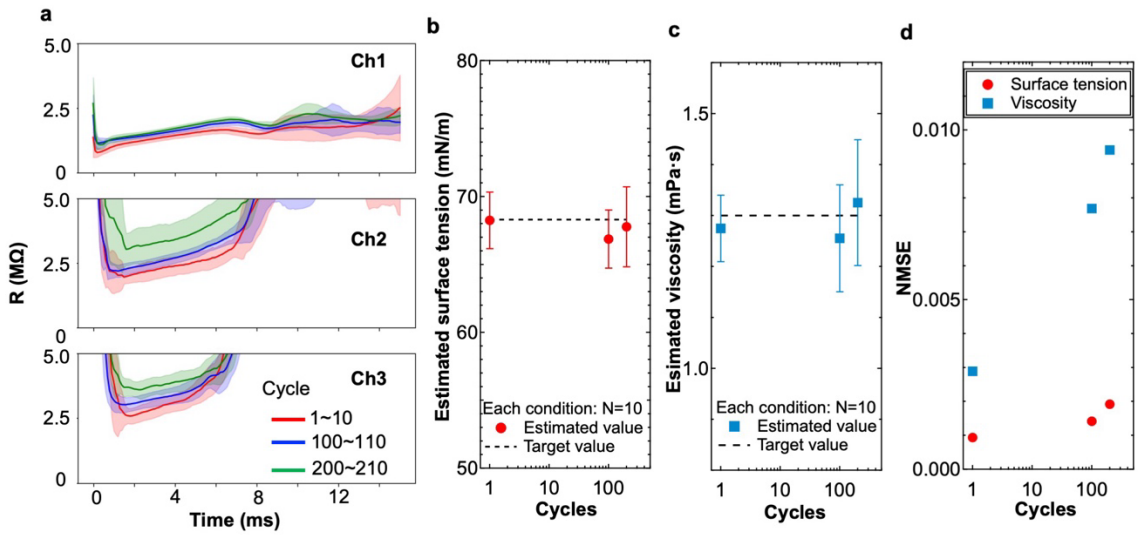

Figure S10. Sensor stability under continuous droplet impact. (a) Time-series resistance changes with standard deviation for each channel (Ch1, Ch2, and Ch3) under continuous droplet impact of 10 wt% glycerol. Comparisons of (b) estimated surface tension values and (c) estimated viscosity values under continuous droplet impact of 10 wt% glycerol. (d) Changes in NMSE of surface tension and viscosity under continuous droplet impact of 10 wt% glycerol.

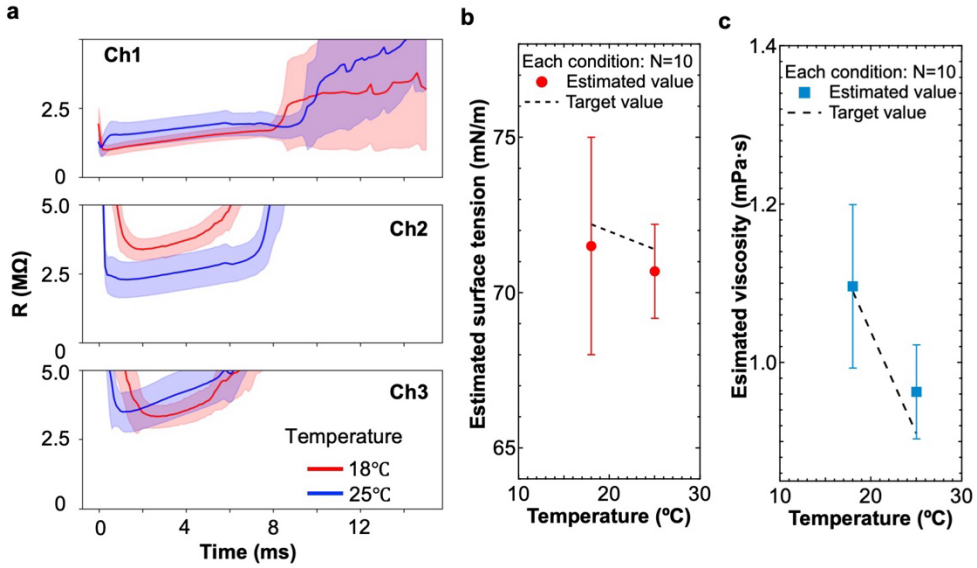

Figure S11. Temperature dependence. (a) Time-series resistance changes with standard deviation for each channel (Ch1, Ch2, and Ch3) at approximately 18℃ and 25℃ for water. (b) Estimated surface tension values and (c) estimated viscosity values at approximately 18℃ and 25℃ for water.